

## Chapter 6

---

# EMPIRICAL PERFORMANCE MODELS BASED ON TWO-DIMENSIONAL CASCADE TESTS

---

The theoretical methods to analyze the flow in cascades presented in Chapter 5 are useful design and analysis methods, but they are not sufficient for day-to-day axial-flow compressor design activity. The many limitations restricting the accuracy and range of application of those methods have been discussed in Chapter 5. Consequently, empirical models are commonly used as a means of predicting the basic performance of cascades in axial-flow compressor design and analysis. These empirical models are derived from experimental data obtained from two-dimensional cascade testing. Extensive testing of this type has been accomplished, particularly by the NACA. Rather sophisticated empirical methods are available for the standard blade profiles discussed in Chapter 4. In the case of advanced blade types, such as the controlled diffusion airfoils discussed in Chapter 4, alternate empirical models may be required. Typically these will be an adaptation of the methods used for the standard airfoil profiles, specifically addressing the improved performance characteristics achieved by the new profile design.

The basic objective of the empirical modeling process is to predict the fluid turning and total pressure loss for a cascade under fairly general operating conditions. Also, operating conditions where near-optimum performance can be expected need to be identified by the empirical models. These are often referred to as design conditions, since they are appropriate for use under the compressor's design operating condition where optimum performance is usually desired. Indeed, it will be seen in Chapters 10 and 11 that these can be used as a basis for selecting blade geometry to match the desired flow field through the compressor. Special empirical models to address blade tip leakage and seal leakage through stator shroud seals will also be covered in this chapter.

## NOMENCLATURE

- $a$  = distance to point of maximum camber along chord  
 $B_{wake}$  = blade wake blockage

- $b$  = exponent factor in Eq. (6-21); also distance from chord line to the point of maximum camber  
 $C$  = absolute velocity  
 $C_c$  = seal carryover coefficient  
 $C_r$  = seal contraction ratio  
 $C_t$  = seal throttling coefficient  
 $C_{l0}$  = lift coefficient  
 $c$  = blade chord  
 $D$  = diffusion factor in Eq. (6-29)  
 $D_{eq}$  = equivalent diffusion factor  
 $h$  = blade height  
 $i$  = incidence angle  
 $K_{sh}$  = blade shape parameter  
 $K_{t,i}$  = design incidence angle thickness correction factor  
 $K_{t,\delta}$  = design deviation angle thickness correction factor  
 $M$  = Mach number  
 $M_c$  = critical Mach number  
 $m$  = slope parameter in Eq. (6-19)  
 $\dot{m}$  = mass flow rate  
 $N$  = number of seal fins  
 $N_{row}$  = blade row number (sequential through the compressor)  
 $n$  = slope parameter in Eq. (6-12)  
 $o$  = throat opening  
 $P$  = pressure  
 $p$  = seal pitch, Fig. 6-22  
 $R$  = range from design inlet angle to stall angle, gas constant or radius of curvature  
 $Re_c$  = blade chord Reynolds number  
 $r$  = radius  
 $s$  = blade pitch  
 $T$  = temperature  
 $t$  = seal point thickness, figure 6-22  
 $t_b$  = blade maximum thickness  
 $U_c$  = leakage velocity  
 $W$  = relative velocity  
 $Z$  = number of blades in a blade row  
 $\alpha$  = angle of attack; also parameter in Eq. (6-38)  
 $\beta$  = flow angle  
 $\chi$  = blade angle with chord  
 $\delta$  = deviation angle  
 $\delta_c$  = blade tip or seal clearance  
 $\gamma$  = stagger angle  
 $\kappa$  = blade angle with the meridional direction  
 $\theta$  = camber angle  
 $\theta_w$  = blade wake momentum thickness  
 $\rho$  = gas density  
 $\phi$  = angle defined in Fig. 6-17  
 $\psi$  = angle defined in Fig. 6-17

$\sigma$  = solidity  
 $\tau$  = torque  
 $\omega$  = rotation speed  
 $\bar{\omega}$  = total pressure loss coefficient

## Subscripts

$c$  = negative stall angle parameter or leakage parameter  
 $m$  = meridional component; also minimum loss condition  
 $max$  = maximum value  
 $s$  = positive stall angle or bow shock wave condition  
 $t$  = total thermodynamic condition  
 $u$  = parameter on upper (suction) blade surface  
 $0$  = zero-camber condition  
 $1$  = parameter at blade inlet  
 $2$  = parameter at blade exit  
 $10$  = parameter for 10% thick profile  
 $\theta$  = tangential component  
 $*$  = sonic flow condition

## Superscripts

$*$  = design condition  
 $'$  = relative condition

## 6.1 CASCADE GEOMETRY AND PERFORMANCE PARAMETERS

Figure 6-1 illustrates the basic parameters and nomenclature used to describe the cascade flow. Subscripts 1 and 2 are used to designate conditions at the inlet and discharge of the blade, respectively. Blades have a chord length,  $c$ , and a tangential spacing between adjacent blade camberlines or pitch,  $s$ . The stagger or setting angle,  $\gamma$ , is the angle between the chord line and the axial direction. The flow enters the cascade with velocity,  $W_1$ , and the flow angle with the axial direction is  $\beta_1$ . The angle between the inlet velocity vector and the chord line is called the angle of attack,  $\alpha$ , i.e.,

$$\alpha = \beta_1 - \gamma \quad (6-1)$$

The flow exits the cascade with velocity,  $W_2$ , and the flow angle with the axial direction is  $\beta_2$ . The blade angles  $\kappa_1$  and  $\kappa_2$  are the angles between the camberline and the axial direction at the leading and trailing edges, respectively. The incidence angle,  $i$ , and the deviation angle,  $\delta$ , are defined as

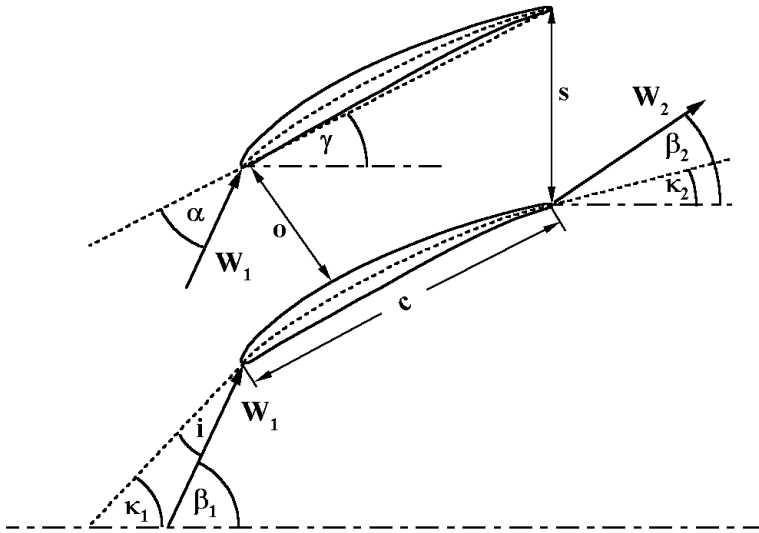


FIGURE 6-1 Cascade Nomenclature

$$i = \beta_1 - \kappa_1 \quad (6-2)$$

$$\delta = \beta_2 - \kappa_2 \quad (6-3)$$

As discussed in Chapter 4, the angles  $\kappa_1$  and  $\kappa_2$  are not well defined for the NACA families of blade camberlines. For this reason, NACA cascade data is usually presented in terms of the angle of attack and the fluid turning,  $\varepsilon$ .

$$\varepsilon = \beta_1 - \beta_2 \quad (6-4)$$

It has become fairly common practice to use an equivalent circular-arc camberline for the NACA 65-series camberline as a basis for defining  $i$ ,  $\delta$ ,  $\kappa_1$  and  $\kappa_2$ , following the procedure described in Chapter 4. Several other parameters will be used in the empirical correlations reviewed in this chapter. The minimum passage opening or throat width,  $o$ , is illustrated in Fig. 6-1. The location of the point of maximum camber,  $a/c$ , is illustrated in Fig. 4-6. The thickness-to-chord ratio,  $t_b/c$ , is illustrated in Fig. 4-1. The solidity,  $\sigma$ , and the camber angle,  $\theta$ , are defined by

$$\sigma = c/s \quad (6-5)$$

$$\theta = \kappa_1 - \kappa_2 \quad (6-6)$$

Equation (4-29) will be used to relate lift coefficient,  $C_{l0}$ , of the NACA camberlines to camber angle, i.e.,

$$\tan(\theta/4) = 0.05515C_{l0}/(a/c) \quad (6-7)$$

## 6.2 DESIGN ANGLE OF ATTACK OR INCIDENCE ANGLE

The design incidence angle,  $i^*$ , or design angle of attack,  $\alpha^*$ , define a near-optimum or minimum-loss inlet angle for the cascade. Figure 6-2 shows a chart of the design angle attack by Herrig et al. (1957) for NACA 65-series blades with solidity and lift coefficient as parameters. The selection of  $\alpha^*$  was based on achieving smooth blade surface pressure distributions, particularly on the suction surface. This writer has formulated the following empirical model based on that design chart.

$$\alpha^* = [3.6K_{sh}K_{t,i} + 0.3532\theta(a/c)^{0.25}]\sigma^e \quad (6-8)$$

$$e = 0.65 - 0.002\theta \quad (6-9)$$

The data in Fig. 6-2 applies to NACA 65-series blades with  $t_b/c = 0.1$ , so  $K_{t,i} = K_{sh} = 1$  and  $a/c = 0.5$ . The parameters  $K_{sh}$  and  $K_{t,i}$  are adapted from the design incidence correlation of Lieblein (1960), which is also presented in NASA SP-36 (Johnsen and Bullock, 1965). Lieblein shows that design incidence angle correlations for NACA 65-series blades with  $t_b/c = 0.1$  can be extended to other profile types and other thickness-to-chord ratios by applying the correction factors to the design incidence (or design angle of attack) for camber angle equal zero.  $K_{sh}$  assumes values of 1.0 for NACA profiles, 1.1 for the C4-series profile and 0.7 for the double-circular-arc profile. Figure 6-3 shows the correction term  $K_{t,i}$

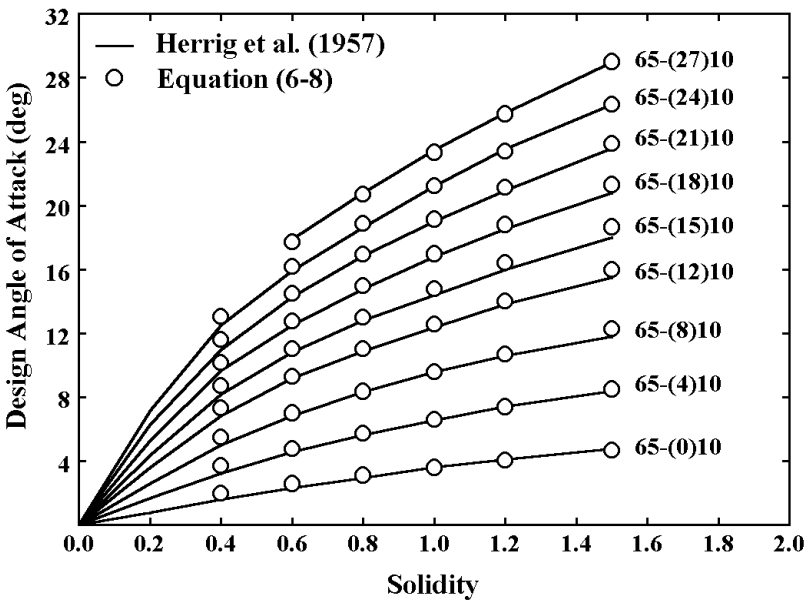


FIGURE 6-2 The Design Angle of Attack

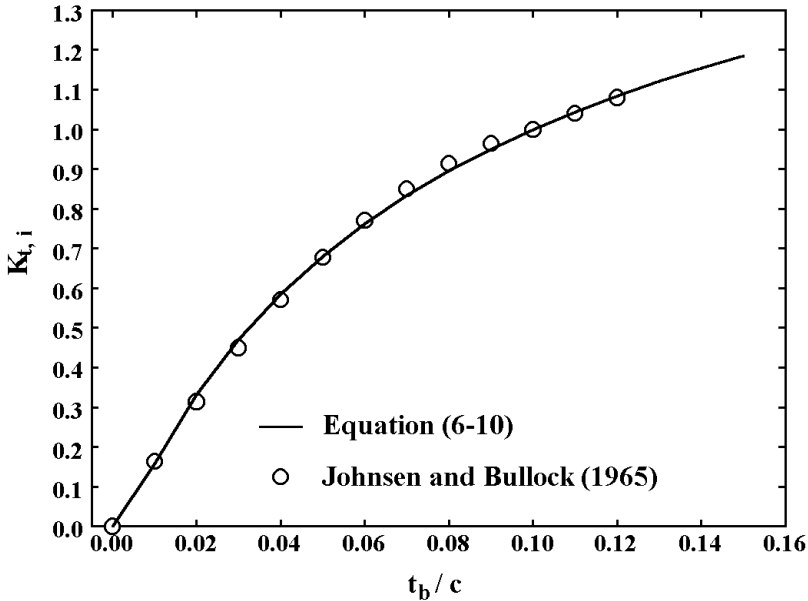


FIGURE 6-3 Thickness Correction for  $\alpha^*$

provided graphically in Johnsen and Bullock (1965), compared to the following empirical equation:

$$K_{t,i} = (10t_b / c)^q \quad (6-10)$$

$$q = 0.28 / [0.1 + (t_b / c)^{0.3}] \quad (6-11)$$

The parameter  $a/c$  introduced into Eq. (6-8) serves to extend the correlation to the NACA A<sub>4</sub>K<sub>6</sub> inlet guide vane camberline, and is presumed to be applicable to the parabolic-arc camberline also, although experimental data isn't available for the writer to actually confirm that.

Lieblein's (1960) design incidence angle correlation is developed from basically the same data as that in Fig. 6-3, but with the intent to identify the minimum loss incidence angle. The equivalent circular-arc camberline is used for the NACA 65-series blades as the basis for defining the incidence angle. The form of Lieblein's correlation is

$$i^* = K_{sh} K_{t,i} (i_0^*)_{10} + n\theta \quad (6-12)$$

The first term on the right-hand side of Eq. (6-12) is the design incidence angle for a camber angle of zero. It is computed from a correlation for NACA 65-series blades with  $t_b / c = 0.1$ , corrected by  $K_{sh}$  and  $K_{t,i}$ . The base zero-camber incidence

angle graphical correlation from Johnsen and Bullock (1965) is shown in Fig. 6-4, along with predictions from the following empirical equations developed from the graphical correlation.

$$(i_0^*)_0 = \frac{\beta_1^p}{5 + 46 \exp(-2.3\sigma)} - 0.1\sigma^3 \exp[(\beta_1 - 70)/4] \quad (6-13)$$

$$p = 0.914 + \sigma^3 / 160 \quad (6-14)$$

Figure 6-5 shows the graphical correlation for the slope factor,  $n$ , from Johnsen and Bullock (1965) along with predictions from the following empirical equation:

$$n = 0.025\sigma - 0.06 - \frac{(\beta_1 / 90)^{(1+1.2\sigma)}}{1.5 + 0.43\sigma} \quad (6-15)$$

It can be noted that both Eqs. (6-13) and (6-15) contain the flow angle, which is, itself, a function of  $i^*$ . Hence, an iterative solution is needed to compute the design incidence angle using Lieblein's (1960) correlation. Lieblein's model applies only to blades where  $a/c = 0.5$ . To treat the NACA A<sub>4</sub>K<sub>6</sub> guide vanes and parabolic-arc blades, this writer has used the following procedure. A pseudo-blade inlet angle is computed as

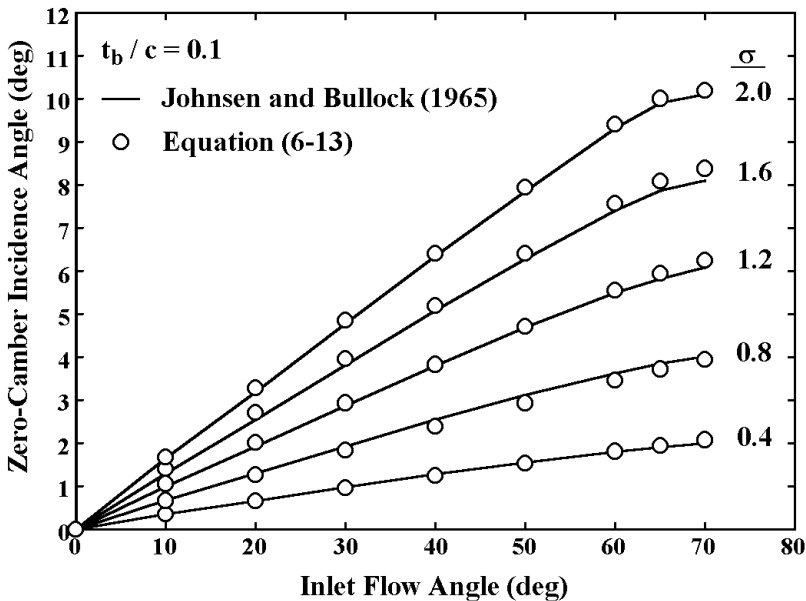


FIGURE 6-4 Zero-Camber Design Incidence Angle

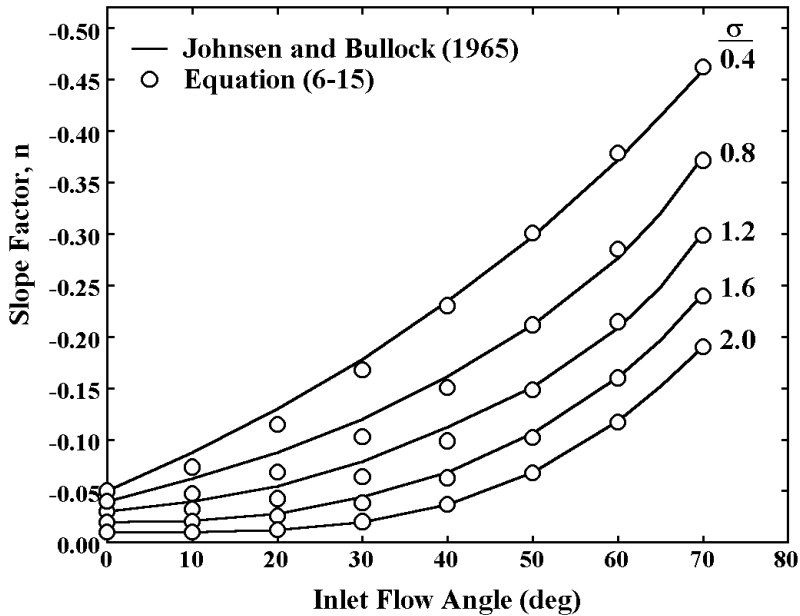


FIGURE 6-5 Design Incidence Angle Slope Factor

$$\bar{\kappa}_1 = |\gamma| + \frac{1}{2}\theta \quad (6-16)$$

This is used to compute a pseudo-design incidence angle using Lieblein's correlations. Then, the design angle of attack for the actual blade is adjusted by

$$\alpha^* = \bar{\kappa}_1 + \bar{i}^* - |\gamma| + (a/c - 0.5)\theta \quad (6-17)$$

The actual design incidence angle is given by

$$i^* = \alpha^* + \gamma - \kappa_1 \quad (6-18)$$

This writer has used both the design angle of attack correlation of Eq. (6-8) and Lieblein's design incidence models rather extensively in axial-flow compressor aerodynamic performance analysis. Clearly, Lieblein's model is based on a less subjective criterion than  $\alpha^*$  and includes more parameters in the correlation. But, in practice, the design angle of attack model has consistently resulted in more accurate compressor performance predictions. That is not necessarily a significant evaluation of the two models. A performance analysis uses many other empirical models, which are discussed in the remainder of this chapter. Performance prediction accuracy depends on the complete set of models, more than on



any single model. So, all that really can be said is that this writer has had better success using the design angle of attack model.

6.3 DESIGN DEVIATION ANGLE

Lieblein (1960) also supplies an empirical model for the design deviation angle,  $\delta^*$ , corresponding to operation at the design incidence angle. This model is reviewed in somewhat greater detail in NASA SP-36 (Johnsen and Bullock, 1965). The model is similar in form to Lieblein's design incidence angle model, i.e.,

$$\delta^* = K_{sh} K_{t,\delta} (\delta_0^*)_{10} + m \theta \tag{6-19}$$

$K_{sh}$  is the same as for the design incidence angle model. Figure 6-6 shows the graphical form of the base zero-camber deviation angle from Johnsen and Bullock (1965) along with predictions from the following empirical equation:

$$(\delta_0^*)_{10} = 0.01 \sigma \beta_1 + [0.74 \sigma^{1.9} + 3 \sigma](\beta_1 / 90)^{(1.67 + 1.09 \sigma)} \tag{6-20}$$

The slope parameter,  $m$ , is expressed as a function of its value for a solidity of 1.0,  $m_{1.0}$ , corrected for other values of solidity in the following form.

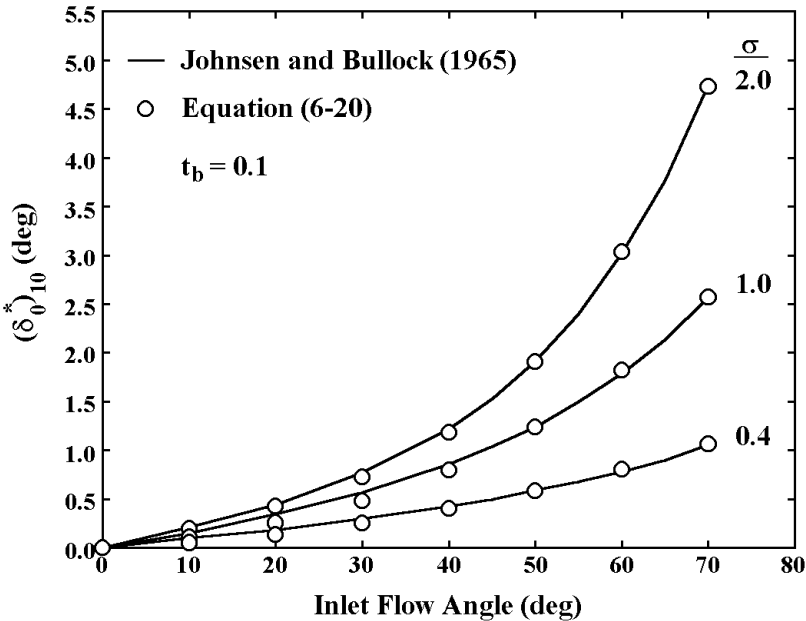


FIGURE 6-6 Zero-Camber Deviation Angle

$$m = m_{1,0} / \sigma^b \quad (6-21)$$

The graphical form of the parameters  $m_{1,0}$ ,  $b$  and  $K_{t,\delta}$  from NASA SP-36 (Johnsen and Bullock, 1965) are shown in Fig. 6-7, 6-8 and 6-9, along with predictions from empirical equations used by this writer. Defining  $x = \beta_I / 100$ , the slope factor for the NACA 65-series camberline is modeled as

$$m_{1,0} = 0.17 - 0.0333x + 0.333x^2 \quad (6-22)$$

For circular-arc camberlines,

$$m_{1,0} = 0.249 + 0.074x - 0.132x^2 + 0.316x^3 \quad (6-23)$$

The exponent,  $b$ , is modeled by

$$b = 0.9625 - 0.17x - 0.85x^3 \quad (6-24)$$

$$K_{t,\delta} = 6.25(t_b / c) + 37.5(t_b / c)^2 \quad (6-25)$$

It can be seen that Lieblein's design deviation angle model does not apply to the NACA A<sub>4</sub>K<sub>6</sub> inlet guide vane or parabolic-arc camberlines. For those blade types,

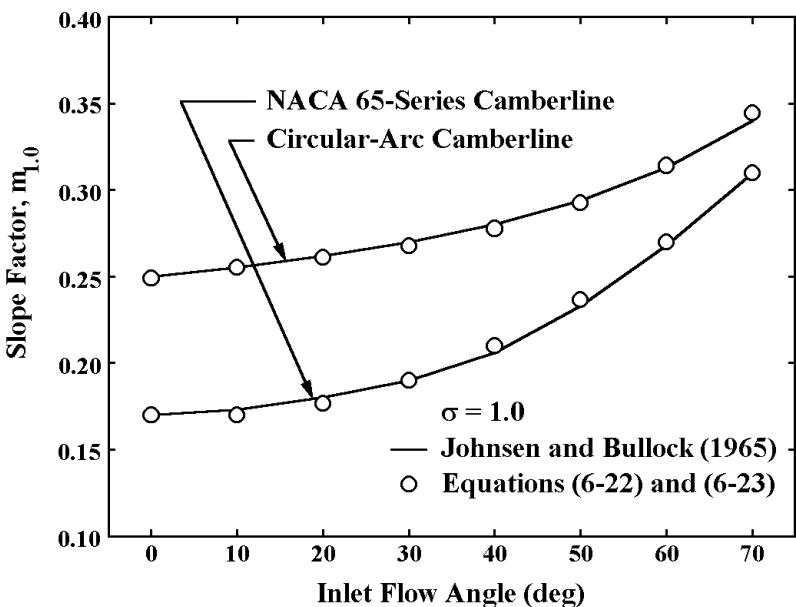


FIGURE 6-7 Design Deviation Angle Slope Factor

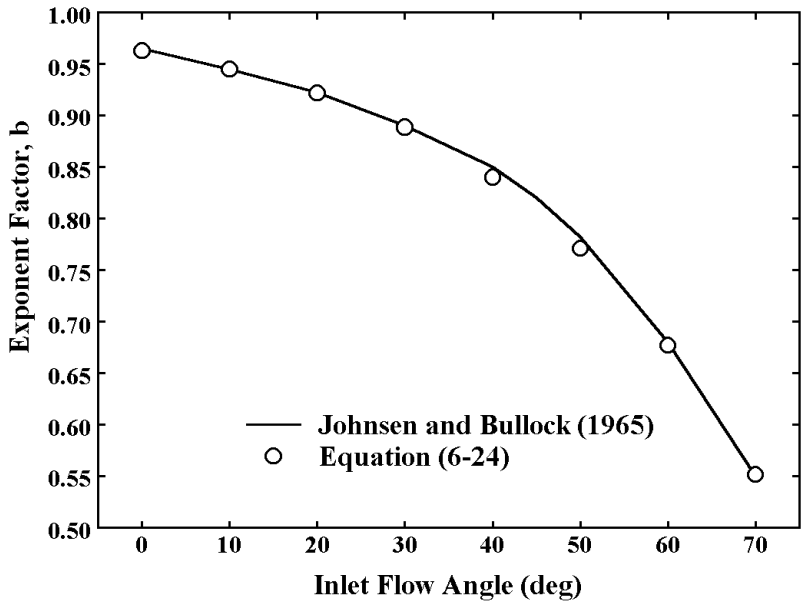


FIGURE 6-8 Design Deviation Angle  $\sigma$  Exponent

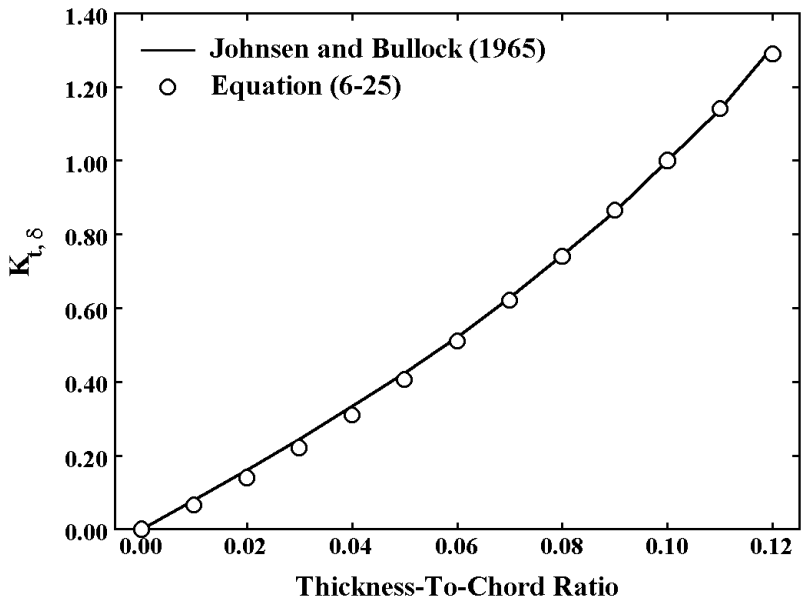


FIGURE 6-9 Thickness Correction for  $\delta^*$

a modified design deviation angle correlation by Howell (1942, 1945) can be used. Howell's correlation is expressed in terms of the discharge flow angle, which is a function of the deviation angle, but that problem is easily remedied by substituting for  $\beta_2$  using Eq. (6-3). Howell also does not account for blade thickness-to-chord and profile shape effects, so it is adjusted using Lieblein's corrections for those effects. The modified form used is

$$\delta^* = \frac{0.92(a/c)^2 + 0.002\kappa_2}{1 - 0.002\theta/\sqrt{\sigma}} \frac{\theta}{\sqrt{\sigma}} + (K_{sh}K_{t,\delta} - 1)(\delta_0^*)_{10} \quad (6-26)$$

Equation (6-26) is also used for all inlet guide vanes, regardless of camberline or profile type. Inlet guide vanes are unique in the sense that they are normally the only cascades in an axial-flow compressor that accelerate the flow. Indeed, at sufficiently large stagger angles, such that the blade passage throat is located at the discharge, they function just like turbine nozzle blade rows. In those cases, an axial-flow turbine deviation angle correlation would be more appropriate. But that is not really a viable approach, since the throat of inlet guide vanes also may be located at the inlet. In the case of adjustable inlet guide vanes, both situations may be encountered in the same compressor. Basically, the function of inlet guide vanes is to turn the flow from an inlet flow angle of zero to some larger flow angle. In the context of a compressor analysis, this means an inlet guide vane will have a negative camber angle. The preceding empirical equations are all applicable to positive camber angles only. They can be applied to a cascade with negative camber simply by changing the signs of all blade angles ( $\theta$ ,  $\gamma$ ,  $\kappa_1$  and  $\kappa_2$ ) and flow angles ( $\beta_1$  and  $\beta_2$ ), applying the correlations, and then changing all signs again to cast the results in the sign convention used for the compressor analysis. When these sign corrections are applied, inlet guide vanes have the unique feature that the corrected  $\gamma$  is negative. Also, the corrected  $\kappa_2$  will have a relatively large negative value. Howell's design deviation angle correlation is the only one known to this writer that can properly handle this situation. Indeed, deviation angles predicted by Eq. (6-26) for the NACA A4K6 inlet guide vane camberline are in rather good agreement with the design charts of Dunavant (1957).

## 6.4 DESIGN LOSS COEFFICIENT AND DIFFUSION FACTORS

Now that a reference or design incidence angle and the corresponding fluid turning or deviation angle have been established, to completely characterize the performance of the cascade at the design operating condition, the corresponding design total pressure loss coefficient has to be predicted. In the context of two-dimensional cascade test results, the loss coefficient involved is referred to as the profile loss coefficient. It is approximately related to the wake momentum thickness,  $\theta_w$  (Lieblein, 1959) by

$$\bar{\omega} = 2 \frac{\theta_w}{c} \frac{\sigma}{\cos \beta_2} \left( \frac{W_2}{W_1} \right)^2 \quad (6-27)$$

Equation (6-27) is similar to Eq. (5-139), except that wake properties rather than boundary layer properties are used. Terms involving the wake shape factor,  $H$ , are neglected, since it is close to unity at typical measuring stations in a cascade test. Velocity relative to the blade,  $W$ , is used for generality, although  $W = C$  for a stationary cascade test. The wake momentum thickness is primarily a function of blade surface skin friction and the blade surface velocity distributions. In particular, the amount of deceleration or diffusion of the surface velocity is a primary factor in determining the wake momentum thickness. In the context of a general blade-loading diagram, this is characterized by the magnitude of the maximum velocity,  $W_{max}$ , relative to the discharge velocity,  $W_2$ . With reference to Fig. 6-10, it can be seen that  $W_{max}$  is primarily a function of  $W_1$ ,  $W_2$  and the blade loading distribution,  $\Delta W$ . For irrotational flow, Stokes' theorem of vector field theory, Eq. (5-12), can be used to show that  $\Delta W$  is a function of the change in the tangential velocity across the blade row, i.e.,

$$\Delta W \propto W_1 + f[(W_{\theta 2} - W_{\theta 1}) / \sigma] \quad (6-28)$$

This fact has been employed to develop various diffusion factors for use as correlating factors for loss coefficient and to estimate the diffusion or loading limits where boundary layer separation leads to an abrupt increase in loss. Two popular diffusion factors are the so-called D-factor,  $D$ , of Lieblein et al. (1953) and the equivalent diffusion factor,  $D_{eq}$ , of Lieblein (1959).

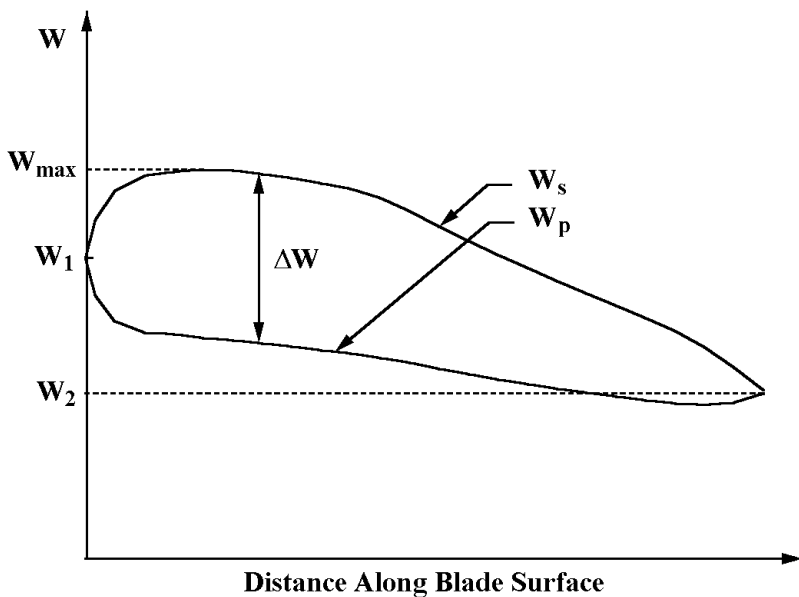


FIGURE 6-10 Typical Blade Loading Diagram

$$D \approx (W_{\max} - W_2) / W_1 \quad (6-29)$$

$$D_{eq} \approx W_{\max} / W_2 \quad (6-30)$$

Equation (6-29) is replaced with a very specific approximation for use as a correlating parameter:

$$D = 1 - \frac{W_2}{W_1} + \frac{W_{\theta 1} - W_{\theta 2}}{2\sigma W_1} \quad (6-31)$$

Johnsen and Bullock (1965) provide a good review of the development of the  $D$ -factor as a correlating parameter. Through comparison with extensive two-dimensional cascade data, it is shown that  $\theta_w / c$  can be well represented by a single curve as a function of  $D$ . From Eq. (6-27) it is expected that loss coefficient should also correlate with  $D$  in the form

$$\frac{\bar{\omega} \cos \beta_2}{2\sigma} \left( \frac{W_1}{W_2} \right)^2 = f(D) \quad (6-32)$$

That has been confirmed by comparison with cascade test data. It is also shown that a correlation can be developed in the form

$$\frac{\bar{\omega} \cos \beta_2}{2\sigma} = f(D) \quad (6-33)$$

The correlation based on Eq. (6-33) offers less resolution than a correlation based on Eq. (6-32), and is far less useful for identifying the loading limit where an abrupt increase in loss is observed. Despite these weaknesses, the correlation form of Eq. (6-33) was adopted. After a correlation of loss coefficient as a function of  $D$  was developed from two-dimensional cascade data, it was evaluated against loss data from annular compressor cascade data. It is found that losses in a compressor cascade are significantly higher than for a simple two-dimensional cascade test. Even at mid-span, where end-wall boundary layer and tip clearance effects should be minimal, three-dimensional effects were found to be significant. Based on the annular cascade data, the two-dimensional cascade correlation was revised to the form shown in Fig. 6-11, which is well approximated by the following empirical equation:

$$\frac{\bar{\omega}^* \cos \beta_2^*}{2\sigma} = 0.0035[1 + 3.5D^* + 37(D^*)^4] \quad (6-34)$$

$D^*$  rather than  $D$  is used to emphasize that the correlation only applies for operation at the design incidence angle. For values of  $D^* > 0.6$ , an abrupt increase in loss is observed, so  $D^* = 0.6$  is adopted as the diffusion limit. Equation (6-34) should not be applied in those cases. The premise of this design loss coefficient

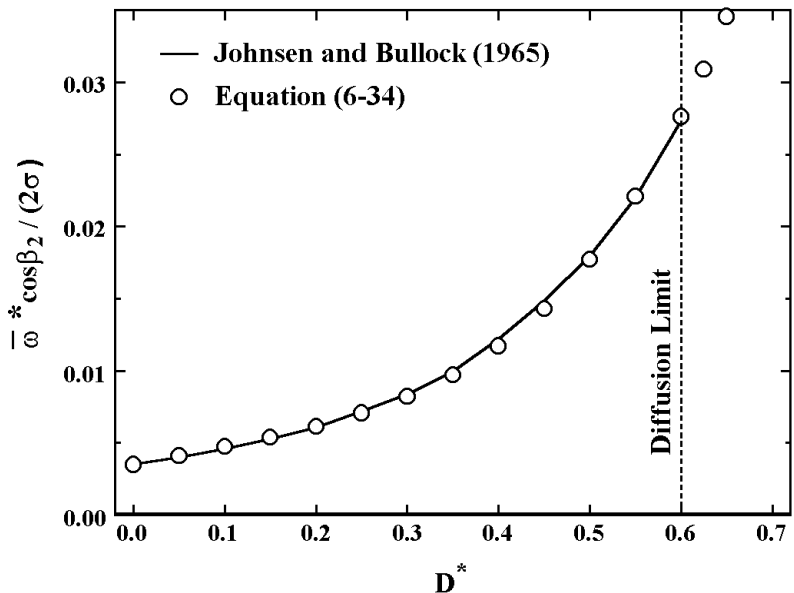


FIGURE 6-11 Loss Coefficient as a Function of  $D^*$

correlation is that well-designed compressor cascades will not operate beyond the diffusion limit at the design incidence condition.

Lieblein (1959) develops the equivalent diffusion factor of Eq. (6-30). From experimental cascade data for NACA 65-series and C.4 circular-arc blades, Lieblein developed the following empirical equation for  $W_{max} / W_l$  for operation at minimum loss, i.e., for operation at the design incidence angle:

$$\left(\frac{W_{max}}{W_l}\right)^* = 1.12 + 0.61 \frac{\cos^2 \beta_1^*}{\sigma} [\tan \beta_1^* - \tan \beta_2^*] \tag{6-35}$$

Hence, the design equivalent diffusion factor is

$$D_{eq}^* = \left(\frac{W_{max}}{W_l}\right)^* \frac{W_1^*}{W_2^*} = \left(\frac{W_{max}}{W_l}\right)^* \frac{\cos \beta_2^*}{\cos \beta_1^*} \frac{W_{m1}}{W_{m2}} \tag{6-36}$$

Lieblein considered only two-dimensional cascades where the axial velocity is constant through the cascade, so he could express Eq. (6-36) in terms of inlet and discharge flow angles only. From two-dimensional cascade data, Lieblein developed an empirical correlation for  $\theta_w / c$  as a function of the equivalent diffusion factor. This can be converted to a correlation of design loss coefficient by applying Eq. (6-27). The result is shown in Fig. 6-12, along with predictions from the following empirical equation.

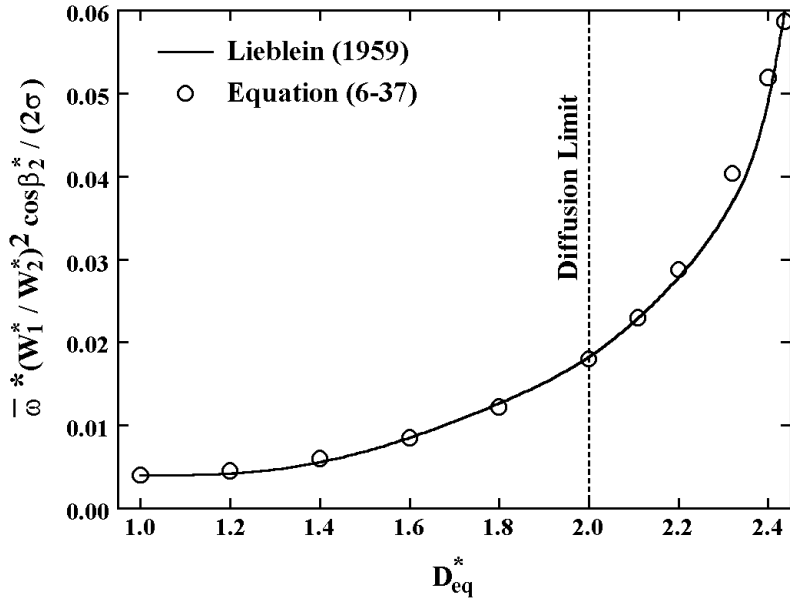


FIGURE 6-12 Loss Coefficient as a Function of  $D_{eq}$

$$\frac{\bar{\omega}^* \cos^2 \beta_2}{2\sigma} \left( \frac{W_1^*}{W_2^*} \right)^2 = 0.004[1 + 3.1(D_{eq}^* - 1)^2 + 0.4(D_{eq}^* - 1)^8] \quad (6-37)$$

It is seen that losses increase rather abruptly for equivalent diffusion factors greater than about 2. Lieblein suggests that an equivalent diffusion factor of 2.0 at design incidence should be considered a diffusion limit, beyond which an abrupt increase in loss can be expected. To permit use of the equivalent diffusion factor as an indicator of the off-design diffusion limit, Lieblein extended Eq. (6-35) to include operation at incidence angles greater than the design incidence angle. The off-design equivalent diffusion factor for  $i \geq i^*$  is computed from Eq. (6-30), using

$$\frac{W_{\max}}{W_1} = 1.12 + 0.61 \frac{\cos^2 \beta_1}{\sigma} [\tan \beta_1 - \tan \beta_2] + \alpha(i - i^*)^{1.43} \quad (6-38)$$

The parameter  $\alpha = 0.0117$  for NACA 65-series blades and  $\alpha = 0.007$  for C4 circular-arc blades. J. Klapproth, in a discussion included in Lieblein (1959), extended these results to include general annular compressor cascades where the axial velocity and radius are not constant, and the cascade may be rotating. The more general form is

$$\frac{W_{\max}}{W_1} = 1.12 + 0.61 \frac{\cos^2 \beta_1}{\sigma} \frac{r_1 C_{\theta 1} - r_2 C_{\theta 2}}{r_1 C_{m1}} + \alpha(i - i^*)^{1.43} \quad (6-39)$$



Equation (6-39) accounts for changes in the meridional velocity and in the blade circulation due to a change in radius and due to blade row rotation. By using this form, the equivalent diffusion factor can be applied to the more typical cases encountered in axial-flow compressor cascades for both design and off-design operation.

In principle, Fig. 6-11 or Fig. 6-12 can be used to estimate the loss coefficient at the design incidence angle. But, in practice, the blade profile loss is only part of the loss that occurs in an axial-flow compressor blade row. Other important sources of the overall total pressure loss include effects due to tip clearance, stator shroud leakage, end-wall boundary layers, Mach number, Reynolds number and secondary flows. Howell (1942, 1945) recognized this fact many years ago and included additional loss models to account for the effects of end-wall and secondary flow losses. Howell expresses these additional losses in terms of drag coefficient,  $C_D$ , where

$$\bar{\omega} = C_D \sigma \cos^2 \beta_1 / \cos^3 \bar{\beta} \quad (6-40)$$

$$\tan \bar{\beta} = (\tan \beta_1 + \tan \beta_2) / 2 \quad (6-41)$$

The end-wall drag coefficient used by Howell is

$$C_{Da} = 0.02s / h \quad (6-42)$$

where  $h$  is the blade height. Howell's secondary flow drag coefficient is based on the blade lift coefficient,  $C_L$

$$C_{Ds} = 0.18C_L^2 \quad (6-43)$$

$$C_L = 2 \cos \bar{\beta} (\tan \beta_1 - \tan \beta_2) / \sigma \quad (6-44)$$

The loss coefficient correlation of Fig. 6-11 presumably includes at least the secondary flow loss, since it is adjusted to reflect the higher losses seen in compressor cascades relative to simple two-dimensional cascades. That is not the case for the correlation in Fig. 6-12. Neither correlation is expected to account for other loss sources listed above. Where possible, these additional losses should be approximated by specific empirical models. Approximate methods to model Mach number effects and tip clearance effects are discussed later in this chapter. Some loss sources can often be neglected, such as Reynolds number effects. Attempts to model end-wall boundary layer losses have been reported in the literature, but none that appear to be particularly general or reliable. It is often more effective to adjust the profile loss models to reflect the higher losses expected in a compressor cascade. Equations (6-34) and (6-37) can be written in the more general form of

$$\frac{\bar{\omega}^* \cos \beta_2^*}{2\sigma} = K_1 [K_2 + 3.5D^* + 37(D^*)^4] \quad (6-45)$$

$$\frac{\bar{\omega}^* \cos \beta_2^*}{2\sigma} \left( \frac{W_1^*}{W_2^*} \right)^2 = K_1 [K_2 + 3.1(D_{eq}^* - 1)^2 + 0.4(D_{eq}^* - 1)^8] \quad (6-46)$$

The parameters,  $K_1$  and  $K_2$ , are empirical constants or functions to be determined by comparing performance predictions with experiment for a suitable number and variety of axial-flow compressors. Their precise form depends on how the performance analysis is formulated, particularly with respect to which loss sources are modeled explicitly and which sources are lumped into  $K_1$  and  $K_2$ . The approach adopted for this writer's performance analysis is discussed at the end of this chapter, along with some variations and alternatives from the literature.

The more general loss coefficient model of Fig. 6-12 or Eq. (6-46) appears to be the better choice. There seems to be some resistance to that choice due to its development from specific blade loading distribution information. It is sometimes argued that its application to other blade camberlines and profiles requires specific blade loading information for development of a new empirical correlation. But that really doesn't justify choosing the model of Fig. 6-11 and Eq. (6-45) instead. In truth, the definition of  $D$  given in Eq. (6-31) has an inherent assumption regarding the blade loading distribution, even though specific blade loading information was not used to define it. There is no reason to believe that  $D$  is a more general parameter than  $D_{eq}$ , when it is applied to blade types different from those for which its loss coefficient empirical model was developed.

## 6.5 POSITIVE AND NEGATIVE STALL INCIDENCE ANGLES

Figure 6-13 is a schematic showing the typical variation of loss coefficient with incidence angle. The loss coefficient is fairly constant over a range of incidence

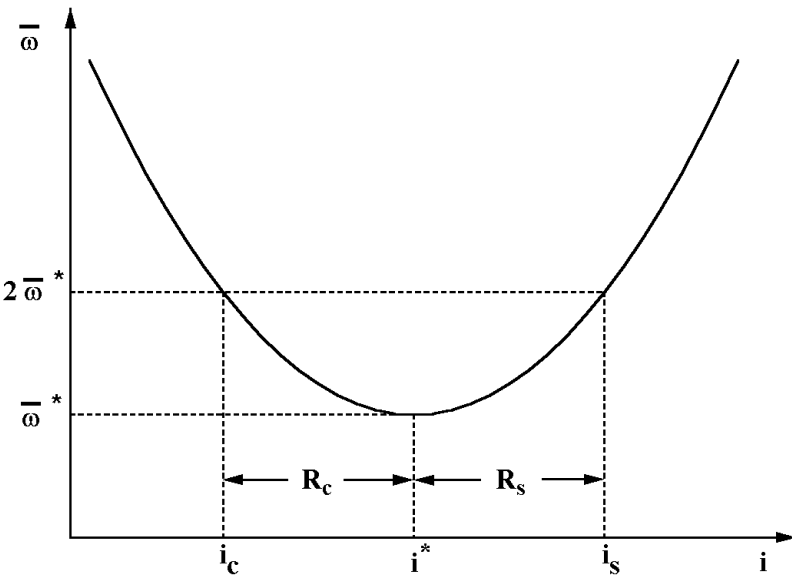


FIGURE 6-13 Off-Design Loss Coefficient

angles near the design incidence angle, but increases rapidly when the cascade is operated too far from the design incidence angle. It is conventional practice to define the limits of low-loss operation by the positive and negative stall incidence angles,  $i_s$  and  $i_c$ , where the loss coefficient becomes twice the minimum loss coefficient, as shown in Fig. 6-13. Herrig et al. (1957) developed an approximate correlation of the positive and negative stall angles of attack for NACA 65-series blades from low Mach number two-dimensional cascade test data. Figure 6-14 shows their correlation along with data computed from the following empirical equations:

$$\alpha_c - \alpha^* = -9 + \left[ 1 - \left( \frac{30}{\beta_{1c}} \right)^{0.48} \right] \frac{\theta}{4.176} \tag{6-47}$$

$$\alpha_s - \alpha^* = 10.3 + \left[ 2.92 - \frac{\beta_{1s}}{15.6} \right] \frac{\theta}{8.2} \tag{6-48}$$

where  $\alpha$ ,  $\beta_l$  and  $\theta$  are all expressed in degrees. Note that Eq. (6-47) is singular if  $\beta_{1c} = 0$ . This writer's practice is to limit  $\beta_{1c} \geq 20^\circ$ . Since  $\alpha$  is a function of  $\beta_l$ , these equations are not directly usable in a performance analysis. But since  $\beta_l = \alpha + \gamma$ , they can be applied by a simple iterative solution. Since  $\alpha - \alpha^*$  is simply the incidence angle range to stall, these empirical models would be expected to be rea-

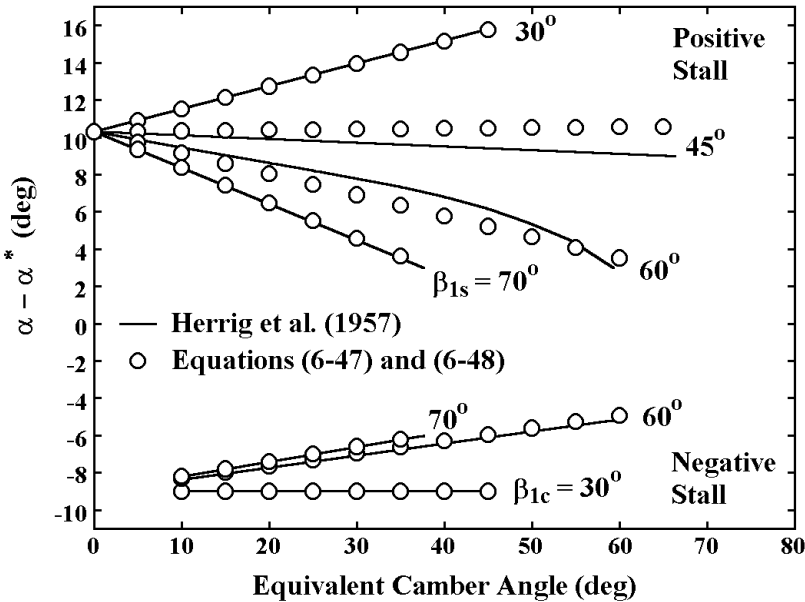


FIGURE 6-14 Stall Angles of Attack

sonable approximations for blade types other than the NACA 65-series. Indeed, they have proven to be effective when used for performance analysis of double-circular-arc blades, which suggests they should be applicable to the C4 circular-arc blades as well. One exception is the NACA A<sub>4</sub>K<sub>6</sub> camberline where cascade test data shows a nearly constant range from the design angle of attack, given approximately by  $\alpha_s - \alpha^* = 10^\circ$  and  $\alpha_c - \alpha^* = -10^\circ$  (Dunavant, 1957). This may suggest that a correction is needed for blades in which the point of maximum camber is not at mid-chord, but it is more likely that the constant incidence ranges to stall is due to the fact that the inlet flow angle is constant for inlet guide vanes. Nevertheless, it should be recognized that the applicability of these empirical models to the parabolic-arc camberline has not been established.

## 6.6 MACH NUMBER EFFECTS

When applying the low-speed cascade empirical correlations to an actual compressor blade row, it is necessary to apply corrections to account for Mach number effects. As Mach number increases, the low-loss working range for the cascade,  $\alpha_s - \alpha^*$  and  $\alpha^* - \alpha_c$ , is reduced relative to the low-speed cascade correlations of Eqs. (6-47) and (6-48). These low-loss working ranges for low-speed cascades will be designated as  $R_s$  and  $R_c$ , i.e.,

$$R_c = \alpha^* - \alpha_c = i^* - i_c \quad (6-49)$$

$$R_s = \alpha_s - \alpha^* = i_s - i^* \quad (6-50)$$

Johnsen and Bullock (1965) note that as Mach number increases ( $i^* - i_c$ ) and ( $i_s - i^*$ ) are reduced by approximately the same amount for moderate Mach number blade profiles such as the NACA 65-series and C4-series blades. But for high Mach number blade profiles such as the double-circular-arc profile, ( $i^* - i_c$ ) is reduced much faster than ( $i_s - i^*$ ) as Mach number increases. This writer computes the negative and positive stall incidence angles for all blade sections by

$$i_c = i^* - R_c / [1 + 0.5M_1^3] \quad (6-51)$$

$$i_s = i^* + R_s / [1 + 0.5(K_{sh} M_1^3)] \quad (6-52)$$

but with the constraint that  $K_{sh} \leq 1$ . The negative stall incidence angle is also required to be no less than the value corresponding to an inlet flow angle for which the mass flow rate is 2% from the blade choke mass flow. An appropriate equation of state from Chapter 2 is used to compute the sonic flow gas density,  $\rho^*$ , and velocity,  $W^*$ , for the local inlet relative total thermodynamic conditions. Assuming the stream sheet thickness is constant between the inlet and the throat, basic conservation of mass yields the inlet flow angle corresponding to choke:

$$\rho_1 W_1 s \cos \beta_{1Choke} = o \rho_* W_* \quad (6-53)$$

This imposes a lower limit on the negative stall incidence angle given by

$$i_c \geq \beta_{1Choke} - \kappa_1 + 1^\circ \quad (6-54)$$

Hence, the approach to choked flow, where  $i$  will be less than  $i_c$ , will be associated with large and rapidly increasing loss coefficients as illustrated in Fig. 6-13. In principle, the loss should become infinite when the passage is choked. But the milder choke condition used here is more appropriate for an axial-flow compressor performance analysis. Blade passage choke is often a local condition along the blade height, which causes a redistribution of the mass flow toward unchoked sections of the blade. If the loss increase near choke is too severe, a numerical solution will often diverge before this redistribution can occur. Beyond that, this simple one-dimensional flow choke calculation is not precise enough to treat it as an absolute limit. The procedure suggested here has been found to be an effective compromise for use in an axial-flow compressor aerodynamic performance analysis.

When these Mach number adjustments are imposed, it may also be necessary to readjust the minimum loss incidence angle and the minimum loss coefficient. Indeed, it is quite possible for the design incidence angle,  $i^*$ , to be less than  $i_c$ . Figure 6-15 illustrates the type of corrections that may be imposed on the off-design loss coefficient at elevated Mach number levels. A minimum loss incidence angle,  $i_m$ , is defined by

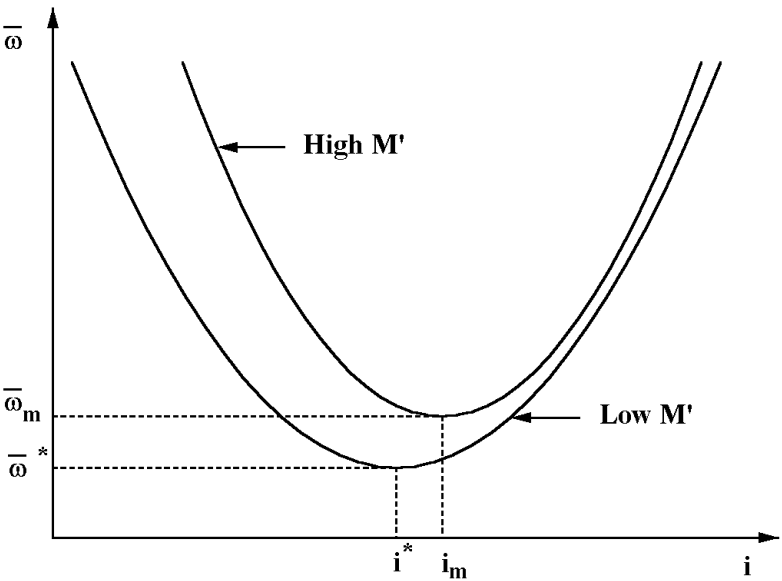


FIGURE 6-15 Mach Number Corrections

$$i_m = i_c + (i_s - i_c)R_c / (R_c + R_s) \quad (6-55)$$

For moderate Mach number blade profiles far from the choked flow limit, it can be seen that  $i_m = i^*$ . But for higher Mach number profiles, or cases where limit in Eq. (6-54) becomes active, Eq. (6-55) results in  $i_m > i^*$ , similar to the schematic shown in Fig. 6-15. As a minimum, the minimum loss coefficient must be adjusted for the difference between  $i_m$  and  $i^*$ , using the low Mach number loss curve directly. For incidence angles between  $i_c$  and  $i_s$ , this writer uses a simple second-order power law relation for the off-design loss coefficient, i.e.,

$$\bar{\omega} = \bar{\omega}_m + \bar{\omega}_m [(i - i_m) / (i_c - i_m)]^2 ; i \leq i_m \quad (6-56)$$

$$\bar{\omega} = \bar{\omega}_m + \bar{\omega}_m [(i - i_m) / (i_s - i_m)]^2 ; i \geq i_m \quad (6-57)$$

It follows directly that the minimum correction required for the minimum loss coefficient is

$$\bar{\omega}_m = \bar{\omega}^* [1 + (i_m - i^*)^2 / R_s^2] \quad (6-58)$$

Except for this fairly minor correction, loss coefficients at the minimum loss incidence show little variation with Mach number until the fluid velocities on the blade surfaces become supersonic. At that point, shock waves can form locally, eventually causing boundary layer separation to significantly increase the minimum loss coefficient. Equation (6-39), applied with  $i = i^*$  and  $\delta = \delta^*$ , defines the maximum velocity,  $W_{max}$ , as illustrated in Fig. 6-10. It follows that the critical Mach number,  $M'_c$ , where the flow first becomes supersonic on the blade surfaces, is given by

$$M'_c = M'_1 W_* / W_{max} \quad (6-59)$$

When the inlet Mach number exceeds the critical Mach number, the minimum loss coefficient is estimated from

$$\bar{\omega}_m = \bar{\omega}^* [1 + (i_m - i^*)^2 / R_s^2] + K_{sh} [(M' / M'_c - 1) W_* / W_1]^2 \quad (6-60)$$

When applying Eq. (6-60), the limit  $M' \leq 1$  is imposed since bow shock wave losses are handled separately, as will be seen in the next section.

## 6.7 SHOCK WAVE LOSS FOR SUPERSONIC CASCADES

The Mach number effects described in the previous section do not account for the additional loss caused by the upstream shock wave when the flow entering the blade row is supersonic. Semi-empirical models to correct for bow shock losses have been reported by Swan (1961) and Miller et al. (1961), both of which

employ essentially identical models. Swan's description is perhaps a little more complete and will be used as the basis for the present discussion. The physics of the problem considered is illustrated in Fig. 6-16. The flow approaches the blade row at a supersonic velocity, passes through an oblique bow shock wave and undergoes a supersonic expansion over the suction surface of the blade. Finally, the expanded, higher Mach number flow passes through the stronger normal shock wave denoted as the passage shock wave in Fig. 6-16. The approach used is to compute the blade surface Mach number modeled as a simple Prandtl-Meyer isentropic expansion. The passage shock loss is then calculated using an upstream Mach number that is the average of the blade inlet Mach number and the expanded flow blade surface Mach number. Here, Swan's (1961) ideal gas model will be generalized somewhat so that it can be used for non-ideal gas equations of state as well. The Prandtl-Meyer expansion is accomplished for a basic double-circular-arc blade profile. The flow is assumed to approach the blade row at a flow angle tangent to the blade suction surface. This is considered fairly representative of the geometry for any profile likely to be used for supersonic inlet flow. And the rather narrow incidence angle operating range expected for supersonic inlet flow also makes the suction surface tangency assumption reasonable. From Figs. 6-16 and 6-17, it is seen that the flow must expand through an angle  $\phi$  along the suction surface. If the blade profile is assumed to have a sharp leading edge, Eqs. (4-7) and (4-10) can be used to define the upper or suction surface of the blade as

$$2R_u / c = \sin(\theta_u / 2) \quad (6-61)$$

$$2b_u / c = \tan(\theta_u / 4) \quad (6-62)$$

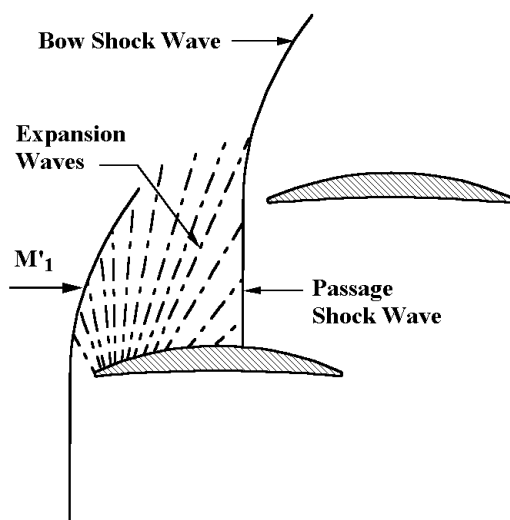


FIGURE 6-16 Shock Wave Loss Model

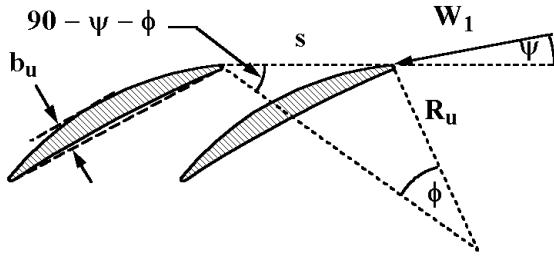


FIGURE 6-17 Expansion Angle Geometry

where  $\theta_u$  is the upper surface “camber angle” and  $R_u$  is the upper surface radius of curvature. Similarly, the mean camberline circular-arc can be expressed by

$$2R/c = \sin(\theta/2) \quad (6-63)$$

$$2b/c = \tan(\theta/4) \quad (6-64)$$

where  $\theta$  is the true camber angle,  $R$  is the camberline radius of curvature, and  $b$  is analogous to  $b_u$  of Fig. 6-17, but for the mean camberline. Since  $b_u - b = t_b/2$ , as can be seen in Fig. 4-8, it follows that

$$\tan(\theta_u/4) = \tan(\theta/4) + t_b/c \quad (6-65)$$

For a circular-arc, the angle of the arc with the chord line at the inlet is given by Eq. (4-35), i.e.,

$$\chi_{u1} = \theta_u/2 \quad (6-66)$$

Since the flow angle is assumed to be equal to the suction surface inlet angle, Eqs. (4-32) and (6-66) yield

$$\beta_1 = 90^\circ - \psi = \theta_u/2 + \gamma \quad (6-67)$$

$$\psi = 90^\circ - \theta_u/2 - \gamma = 90^\circ - \theta_u/2 - \kappa_1 + \theta/2 \quad (6-68)$$

where  $\gamma$  is the blade stagger angle and  $\kappa_1$  is the blade inlet angle, as shown in Fig. 6-1. The law of sines and basic trigonometry applied to the triangle shown in Fig. 6-17 yields

$$\tan \phi = \frac{s \cos \psi}{s \sin \psi + R_u} \quad (6-69)$$



Swan (1961) develops Eq. (6-69) in a more general form by including the leading edge nose radius. That is a relatively insignificant effect, considering the approximate nature of the model. Hence, the assumption of a sharp leading edge is used here to avoid the need to specify the blade nose radius for an aerodynamic performance analysis.

The blade surface Mach number,  $M'_S$ , and velocity,  $W_S$ , entering the passage shock wave is given by the well-known Prandtl-Meyer isentropic expansion through the expansion angle  $\phi$ . In general form, this can be expressed as

$$\phi = \int_{W_1}^{W_S} \sqrt{M'^2 - 1} \frac{dW}{W} \quad (6-70)$$

For thermally and calorically perfect gases, this equation can be integrated analytically and expressed in terms of the Prandtl-Meyer angle, which is usually designated as  $\nu(M)$ . To permit use of the model for any appropriate equation of state, Eq. (6-70) must be integrated numerically, noting that the Prandtl-Meyer expansion is an isentropic process.

The shock wave total pressure loss is calculated for a normal shock wave with an inlet Mach number of

$$M'_{in} = \sqrt{M'_1 M'_S} \quad (6-71)$$

Again, for thermally and calorically perfect gases, the total pressure loss across a normal shock wave can be expressed analytically. To generalize the calculation for any appropriate equation of state, a numerical solution is required. This involves simple conservation of mass, momentum and energy across the shock wave in the form

$$(\rho W)_{in} = (\rho W)_{out} \quad (6-72)$$

$$(P + \rho W^2)_{in} = (P + \rho W^2)_{out} \quad (6-73)$$

$$H_{in} = H_{out} \quad (6-74)$$

$$s_{out} \geq s_{in} \quad (6-75)$$

Equations (6-72) through (6-74) can be solved by simple iteration, noting that the flow downstream of the shock wave is subsonic. Equation (6-75) requires that the second law of thermodynamics be satisfied as stated in Eq. (2-6). Then the downstream total pressure is calculated to yield the desired total pressure loss across the shock wave.

## 6.8 OFF-DESIGN CASCADE PERFORMANCE CORRELATIONS

The calculation of loss and fluid turning at off-design incidence angles is more complex than for the design incidence angle. Although two-dimensional cascade

test data provide some useful guidance, the off-design performance of an annular cascade in an axial-flow compressor is far more complex. Successive blade rows in a compressor are normally closely spaced, resulting in significant interaction between them. Two-dimensional cascade test data is based on measurements rather far downstream where blade wakes and flow distortion is minimal. That is far from the case encountered in a compressor. Rotating stall can significantly influence the flow in a compressor cascade, particularly when the compressor operates at rotation speeds well below its design speed. Two-dimensional cascade test data provides no insight into this phenomenon. A very fundamental difference between compressor cascades and cascade testing is the fact that the flow is far from two-dimensional in the compressor. In a compressor, significant changes in axial velocity and radius across the cascade are common and end-wall boundary layers often influence a substantial portion of the flow field. By contrast, substantial effort is made to minimize these effects in two-dimensional cascade tests, typically by use of boundary layer suction.

Consequently, off-design blade row performance empirical model development requires calibration against axial-flow compressor performance data, including a range of compressor types and operating conditions. It follows that these empirical models are substantially influenced by the overall strategy used for the compressor performance analysis. In effect, it soon becomes impossible to separate the parts from the whole. Numerous approximations are required to model the through-flow, end-wall boundary layers, tip clearance, shroud leakage, etc., in a performance analysis. It is important to recognize that the off-design empirical correlations suggested here are simply methods that have been found effective in the context of this writer's performance analysis as it is described in this book.

The blade row incidence angle and the axial velocity ratio across the cascade significantly influence the off-design deviation angle. Johnsen and Bullock (1965) provide an empirical model for variation of the deviation angle with incidence angle at the design incidence angle. This graphical correlation is shown in Fig. 6-18, along with predictions from the following empirical equation:

$$\left[ \frac{\partial \delta}{\partial i} \right]^* = [1 + (\sigma + 0.25\sigma^4)(\beta_1 / 53)^{2.5}] / \exp(3.1\sigma) \quad (6-76)$$

G. Mellor has developed plots of  $\beta_2$  as a function of  $\beta_1$  from NACA cascade data (see Fig. 3.9, Horlock, 1958). These are equivalent to plots of  $\delta$  versus  $i$ . A schematic typical of Mellor's constant-stagger angle characteristics is shown in Fig. 6-19. It can generally be concluded that the deviation angle approaches a constant value near the negative stall incidence angle. At the positive stall incidence angle, the slope of the  $\beta_2$  versus  $\beta_1$  curves approaches unity. For some time, this writer used these two observations and Eq. (6-76) in several unsuccessful attempts to construct a general deviation angle correlation as a function of incidence angle to match the observed behavior at  $i_c$ ,  $i^*$  and  $i_s$ , as suggested by Novak (1973). While this produced reasonable results for certain applications and operating conditions, definite exceptions seemed to always exist where this type of model could not match actual compressor performance data. The requirement

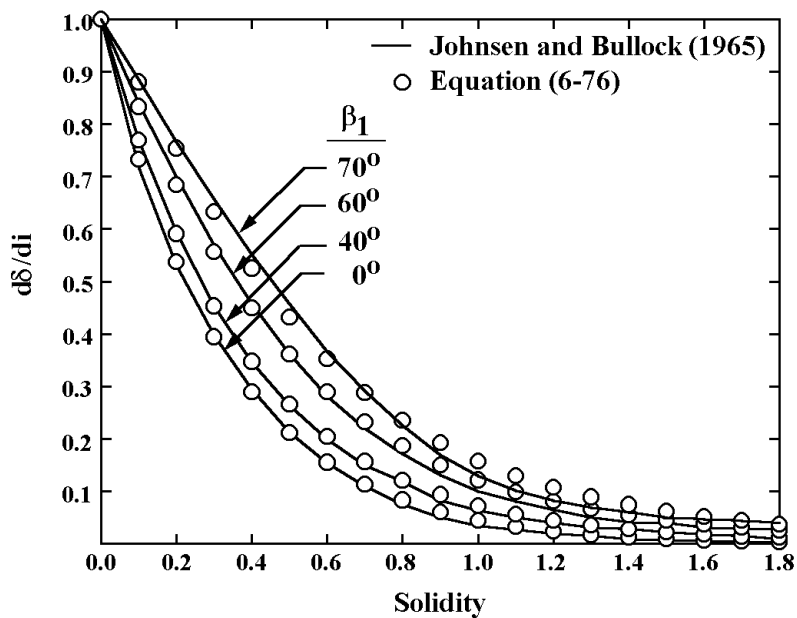


FIGURE 6-18 Off-Design Deviation Slope

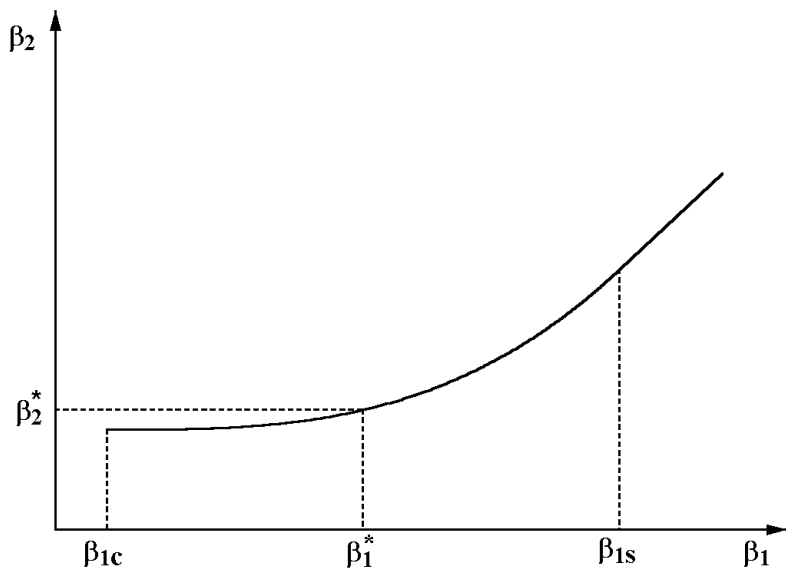


FIGURE 6-19 Schematic of  $\beta_2$  Versus  $\beta_1$  in Cascades

that the fluid turning does not increase with incidence beyond the positive stall incidence angle is particularly troublesome when analyzing the performance of compressors. While this appears to be the case in cascade test results, it does not permit predicting compressor performance at some of the very severe incidence angles at which they are often capable of operating. After experimenting with various modifications and limits, a somewhat arbitrary model was tried, assuming a linear variation of deviation angle with incidence angle with a slope given by Eq. (6-76). This produced such a dramatic improvement in the accuracy and versatility of the compressor performance analysis that the attempt to define a more general empirical correlation was abandoned. The axial velocity ratio across the cascade also has a definite influence on the deviation angle. The correction developed by Pollard and Gostelow (1967) from cascade test results is about as good as any, although it is based on rather limited evidence. Combining their axial velocity correction with the assumed linear variation of deviation angle with incidence angle results in the expression used by this writer for off-design deviation angle prediction.

$$\delta = \delta^* + \left[ \frac{\partial \delta}{\partial i} \right]^* (i - i^*) + 10(1 - W_{m2} / W_{m1}) \quad (6-77)$$

where  $i$  and  $\delta$  are expressed in degrees. Inlet guide vanes require special treatment. It was noted previously in this chapter that inlet guide vanes usually function like turbine nozzle blade rows, where the throat area at the blade discharge largely dictates the discharge flow angle. Hence, the second term on the right-hand side of Eq. (6-77) is omitted for inlet guide vanes, such that deviation angle is not influenced by incidence angle. This is an important feature when compressors employ adjustable inlet guide vanes. In those cases, the vanes may be operated at extremely large incidence angles. Comparison of predicted and measured performance of those types of axial-flow compressors shows no evidence of any incidence angle influence on the deviation angle of the inlet guide vanes.

Figure 6-20 illustrates the model used for off-design loss coefficient. Define a normalized incidence angle parameter as

$$\xi = (i - i_m) / (i_s - i_m); \quad i \geq i_m \quad (6-78)$$

$$\xi = (i - i_m) / (i_m - i_c); \quad i < i_m \quad (6-79)$$

Designating the upstream shock wave loss coefficient (if any) by  $\bar{\omega}_s$ , the off-design loss coefficient is given by

$$\bar{\omega} = \bar{\omega}_s + \bar{\omega}_m[1 + \xi^2]; \quad -2 \leq \xi \leq 1 \quad (6-80)$$

$$\bar{\omega} = \bar{\omega}_s + \bar{\omega}_m[5 - 4(\xi + 2)]; \quad \xi < -2 \quad (6-81)$$

$$\bar{\omega} = \bar{\omega}_s + \bar{\omega}_m[2 + 2(\xi - 1)]; \quad \xi > 1 \quad (6-82)$$

As noted in Fig. 6-20, Eqs. (6-81) and (6-82) are simple linear extrapolations of Eq. (6-80) outside of its designated range of application. The values of the loss

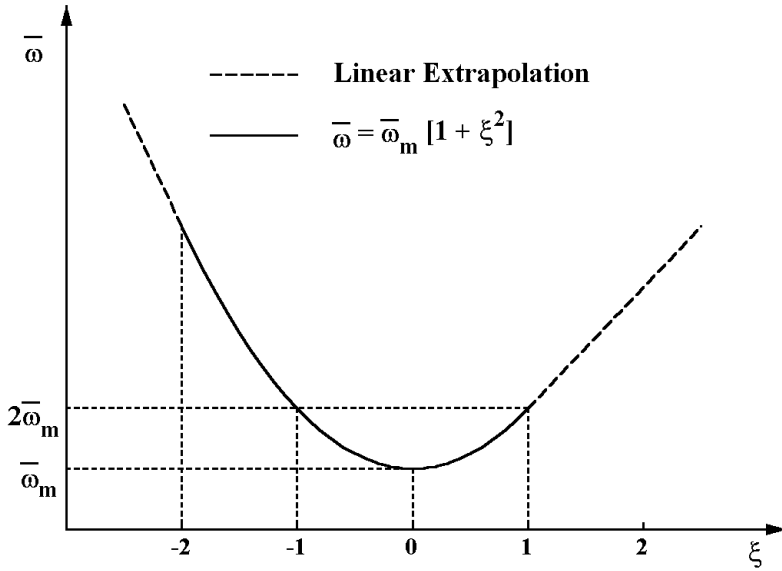


FIGURE 6-20 Off-Design Loss Coefficient

coefficients at  $i_c$ ,  $i_m$  and  $i_s$  are consistent with the definitions of those incidence angles established earlier in this chapter. The remainder of the correlation is completely empirical, based on optimizing the performance prediction accuracy for a wide range of axial-flow compressor types and operating conditions. The lower limit imposed on Eq. (6-80) is largely a safety feature, since operation at such large negative incidence angles is almost never encountered. By contrast, the upper limit imposed on Eq. (6-80) and the extrapolation defined by Eq. (6-82) are essential, and are commonly encountered, particularly when an axial-flow compressor operates at speeds well below its design speed. Limiting the rate of increase in loss coefficient with incidence angle in these conditions really compensates for the fact that the compressor is likely to operate in rotating stall. These stall zones effectively block some of the blade passages such that the incidence angles are not as large as those indicated by an ideal, axisymmetric flow analysis. This writer's performance analysis makes further provision for this type of operation by imposing an area blockage,  $B_{wake}$ , due to the blade wakes. This is based on the blade loading level indicated by Lieblein's equivalent diffusion factor evaluated at off-design conditions, i.e., using the off-design incidence and deviation angles in Eq. (6-39) to compute the off-design equivalent diffusion factor using Eq. (6-30). The wake blockage is given by

$$B_{wake} = 0; D_{eq} \leq 2 \tag{6-83}$$

$$B_{wake} = 1 - (2 / D_{eq})^{0.9}; D_{eq} > 2 \tag{6-84}$$

It will be seen later in this book that the through-flow analysis interprets  $B_{wake}$  as the fraction of the stream sheet area that is unavailable for through flow.

## 6.9 BLADE TIP CLEARANCE LOSS

The calculation of the blade tip clearance loss is based on the same semi-empirical model used for centrifugal compressor impellers in Aungier (2000). Figure 6-21 shows the tip clearance geometry for a typical rotor blade. The situation for unshrouded stator blades is similar, except that the clearance lies along the hub contour. The pressure difference on the two sides of the blade produces a leakage flow through the clearance gap, basically dissipating the pressure difference. The pressure difference across the blade must balance the blade torque as given in Eq. (3-7). For the clearance gap, this can be expressed as

$$\tau = \pi \delta_c [(r \rho C_m)_1 + (r \rho C_m)_2] [r_2 C_{\theta 2} - r_1 C_{\theta 1}] \quad (6-85)$$

The average pressure difference across each blade in the blade row is

$$\Delta P = \tau / (Z r_{tip} \delta_c \cos \gamma) \quad (6-86)$$

where  $Z$  is the number of blades in the blade row. The fluid velocity of the leakage flow is estimated from  $\Delta P$  and the assumed throttling coefficient of Aungier

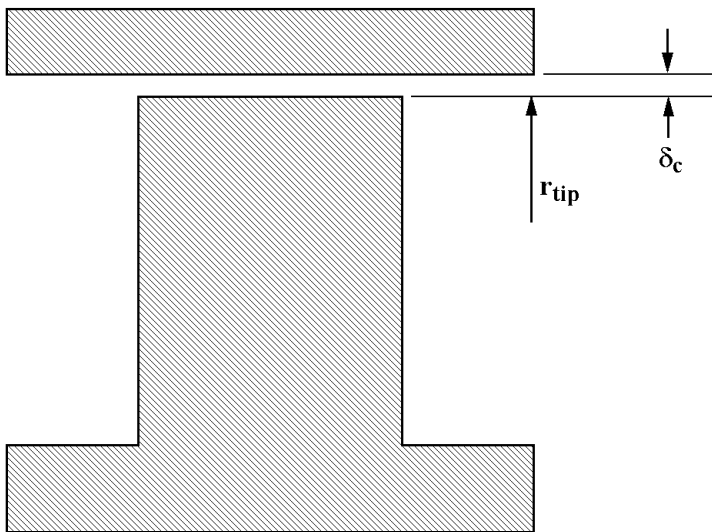


FIGURE 6-21 Blade Tip Clearance Geometry

(2000) for the first blade row, but is reduced as the blade row number,  $N_{row}$ , increases, i.e.,

$$U_c = 0.816 \sqrt{2\Delta P / \bar{\rho}} / N_{row}^{0.2} \quad (6-87)$$

As will be seen in Chapter 8, end-wall boundary layer growth in multistage axial-flow compressors results in a substantial tangential blade force defect, which is expected to reduce the tip leakage flow. The dependence on  $N_{row}$  was determined empirically from comparison of predicted and measured performance of several multistage axial-flow compressors. The leakage mass flow rate is given by

$$\dot{m}_c = \bar{\rho} U_c Z \delta_c c \cos \gamma \quad (6-88)$$

The clearance gap total pressure loss for the entire blade row is

$$\Delta P_t = \Delta P \dot{m}_c / \dot{m} \quad (6-89)$$

This total pressure loss is clearly concentrated in the clearance gap region of the flow field. But if it is applied in that fashion, losses along the end-wall will accumulate from each blade row, eventually causing the through-flow analysis to diverge. The basic problem is that the flow in a multistage compressor undergoes considerable fluid mixing at each blade row due to secondary flows. But a conventional through-flow analysis does not account for this. Hence, once a loss is imposed on a stream sheet in the analysis, it stays on that stream sheet through the remainder of the compressor. To avoid solution divergence, this writer imposes the leakage total pressure loss as a linear distribution across the annulus, such that the integrated  $\Delta P_t$  is equal to the value given by Eq. (6-89), but the total pressure loss is zero at the wall opposite from the clearance gap. Since successive blades encounter clearance (or shroud seal leakage) losses on alternate end-wall contours, this produces a mild concentration of these losses near the end-walls, but with about half of the loss applied at mid-passage. Experience has shown that this yields a stable performance analysis that correlates well with overall compressor experimental performance data.

## 6.10 SHROUD SEAL LEAKAGE LOSS

Figure 6-22 illustrates an alternate style of blade tip geometry that is often used on stator blade rows. Here a shroud band is attached integral with the blades. Typically seal fins are attached to the shroud band to reduce the clearance gap leakage flow, yet protect the compressor from serious damage in the event that a rotor excursion should cause the shaft to come in contact with the shroud. The seal allows larger clearances between the shroud band and the shaft to be used without causing excessive leakage. If contact occurs, the seal strips will be sacrificed, but the more expensive components should be undamaged.

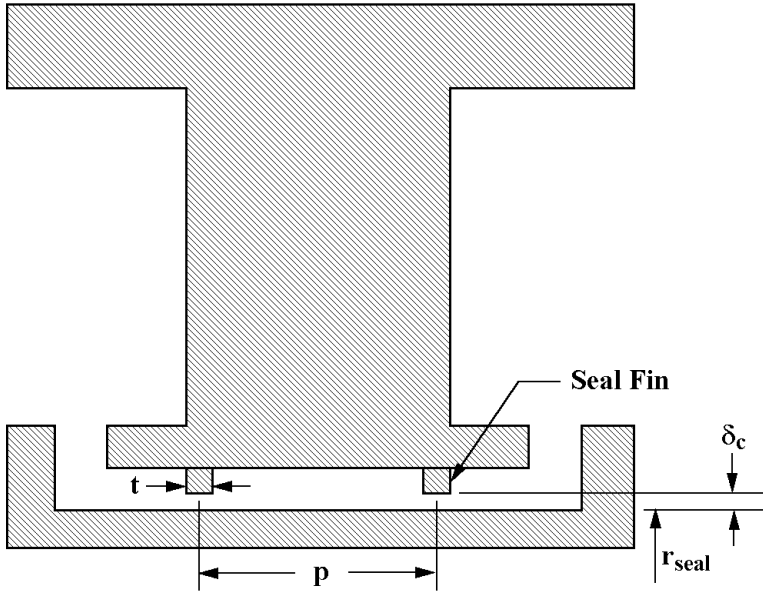


FIGURE 6-22 Shroud Seal Geometry

The total pressure loss due to shroud leakage is that given by the leakage mass flow and the pressure difference across the blade row, i.e.,

$$\Delta P_t = \Delta P \dot{m}_{\text{leak}} / \dot{m} \quad (6-90)$$

This total pressure loss is distributed across the annulus in exactly the same fashion as the tip clearance loss. The leakage mass flow through the labyrinth seal can be computed by the method of Egli (1935), who expresses the leakage mass flow in the form

$$\dot{m}_{\text{leak}} = 2\pi r_{\text{seal}} \delta_c C_t C_c C_r \rho \sqrt{RT} \quad (6-91)$$

Aungier (2000) provides general empirical equations to approximate the coefficients in Egli's model. Here, a simplified model can be used, since the number of fins,  $N$ , in a shroud seal is always relatively small. The contraction ratio is approximated by

$$C_r = 1 - \frac{1}{3 + \left[ \frac{54.3}{1 + 100\delta_c / t} \right]^{3.45}} \quad (6-92)$$



If  $P_R$  designates the ratio of the lower pressure to higher pressure across the seal, the throttling coefficient is approximated by

$$C_t = \frac{2.143 \ln(N) - 1.464}{N - 4.322} [1 - P_R]^{(0.375 P_R)} \quad (6-93)$$

If  $N \leq 12$ , the carryover coefficient is approximated as

$$C_c = 1 + \frac{X_1 [\delta_c / p - X_2 \ln(1 + \delta_c / p)]}{1 - X_2} \quad (6-94)$$

$$X_1 = 15.1 - 0.05255 \exp[0.507(12 - N)] \quad (6-95)$$

$$X_2 = 1.058 + 0.0218N \quad (6-96)$$

Equation (6-94) yields a maximum when  $\delta_c / p = X_2 - 1$ . This represents a poor seal design, which exceeds the range of Egli's model. It is rarely encountered, but it is wise to require  $\delta_c / p \leq X_2 - 1$  when applying Eq. (6-94). Aungier (2000) provides a more detailed discussion and the extension of the empirical equations to  $N > 12$ .

## 6.11 IMPLEMENTATION, EXTENSIONS AND ALTERNATE METHODS

Integration of empirical performance models into an axial-flow compressor performance analysis is by no means a trivial process. Chapters 7 and 8 discuss the through-flow analysis and end-wall boundary layer analysis, which are the other two important components of an aerodynamic performance analysis. It is convenient to discuss the component parts of the performance analysis individually, but the parts cannot really be separated from the whole. An objective of this book is to provide a complete description of the methods used by the author. Completion of the description of the empirical loss models requires a definite qualification. The final adjustments suggested here depend on the other components of the performance analysis to be discussed in the next two chapters, as well as on the use of the complete set of empirical models reviewed in this chapter. The final adjustments may be ineffective if used in a different context.

To complete this discussion, the parameter,  $K_1$  and  $K_2$ , in Eq. (6-46) must be provided. These parameters adjust the profile loss model to compensate for loss sources not specifically modeled here, such as end-wall and secondary flow losses. In the simplest form,  $K_1$  and  $K_2$  may be considered as empirical constants. That is actually not a bad assumption. Rather good performance prediction accuracy has been achieved simply using  $K_1 = 0.004$  and  $K_2 \approx 4$ . That is possible because extremely low values of the aspect ratio are not normally encountered in typical compressors. It is more prudent to include specific provision for aspect ratio effects as suggested by Howell (1942, 1945) in Eq. (6-42). Consider a simple model for skin friction loss in a cascade. If  $c_f$  is the skin friction coefficient, this can be represented by

$$\bar{\omega}_{SF} \propto c_f c / (s \cos \beta_2) \quad (6-97)$$

This can be extended to include an approximate end-wall loss estimate by adding the blade chord-to-height ratio, i.e.,

$$\bar{\omega}_{SF} \propto c_f [c / (s \cos \beta_2) + c / h] \quad (6-98)$$

This simple argument leads to the following expression for  $K_2$ :

$$K_2 = 1 + (s / h) \cos \beta_2 \quad (6-99)$$

The correction is applied to  $K_2$  rather than  $K_1$ , since blade loading is not expected to significantly influence the end-wall loss. By comparison of performance predictions with experiment for a several axial-flow compressors,  $K_1 = 0.0073$ , combined with Eq. (6-99), was found to yield good results, as will be demonstrated in Chapter 9.

It is also useful to include an approximate correction for Reynolds number. Although not normally used in the author's performance analysis, there are extreme cases where a correction may be necessary. The Reynolds number correction is applied only to the skin friction portion of the simple cascade profile loss, as represented by Eq. (6-37). For application to Eq. (6-46), Eq. (6-99) is generalized to the form

$$K_2 = 1 + (\bar{s} / \bar{h}) \cos \beta_2 + 0.004 K_{Re} / K_1 \quad (6-100)$$

For laminar flow ( $Re_c < 2.5 \times 10^5$ ),

$$K_{Re} = \sqrt{2.5 \times 10^5 / Re_c} - 1 \quad (6-101)$$

For turbulent flow ( $Re_c > 2.5 \times 10^5$ ),

$$K_{Re} = \left[ \log(2.5 \times 10^5) / \log(Re_c) \right]^{2.58} - 1 \quad (6-102)$$

These corrections are based on the blade chord Reynolds number,  $Re_c$ , derived from classical Reynolds number formulations for boundary layer skin friction coefficients. The skin friction models used can be found in a variety of books on boundary layer theory, e.g., Schlichting (1968, 1979). These corrections are consistent with the correlation in Fig. 6-12, which is based on data with  $Re_c \approx 2.5 \times 10^5$ . Fig. 6-23 illustrates the basis of this Reynolds number correction. Cascade loss coefficient data from Johnsen and Bullock (1965) are shown as a function of blade chord Reynolds number. The empirical correction curves shown are obtained by normalizing Eqs. (6-101) and (6-102) to the data point closest to  $Re_c = 2.5 \times 10^5$  for each data set.

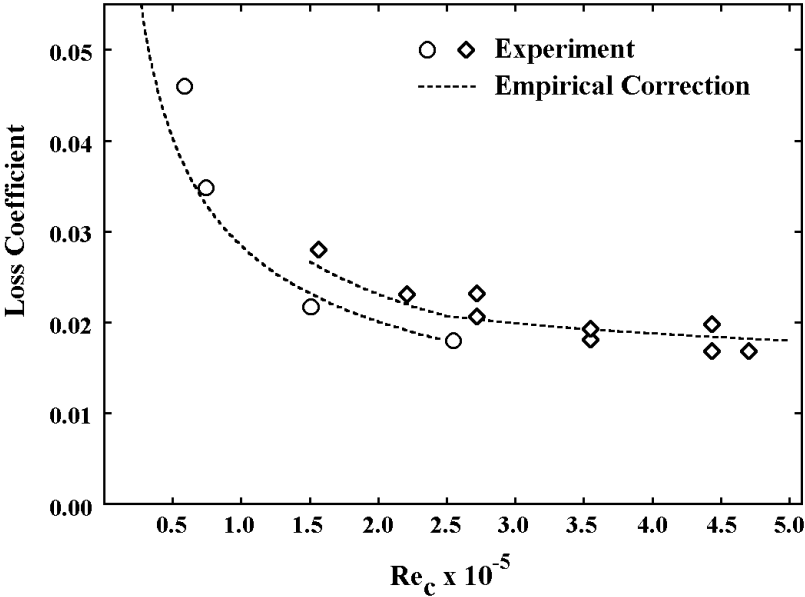


FIGURE 6-23 Reynolds Number Effect

It is appropriate to close this chapter with a reference to an excellent technical paper by Koch and Smith (1976). They present a very careful development of a significant alternate approach to the present methods. Koch and Smith rely on an independent empirical model for end-wall loss and end-wall work formulated from compressor test data. They developed a profile loss model using a compressible boundary layer analysis, including corrections for Mach number, Reynolds number and stream sheet contraction. An alternate model for bow shock loss is also included. Attempts by this author to employ their approach many years ago were unsuccessful, due to the fact that their end-wall loss model simply did not correlate with experimental data for the specific class of axial-flow compressors of interest at the time. But Koch and Smith have shown good agreement with experiment for a significant number of cases, suggesting that this author's experience may not be typical. Indeed, this reference has substantially influenced this author's performance analysis, even though its empirical performance models are not used directly. This will become apparent in Chapter 8 of this book. It is a very significant reference that is highly recommended.

EXERCISES

- 6.1 Consider NACA 65-series blades with  $t_b / c = 0.1$ . Hence,  $a / c = 0.5$  and  $K_{sh} = K_{t,i} = 1$ . Based on Eq. (6-8), what are the independent variables defining the design incidence angle? Repeat for Eq. (6-12).

- 6.2 Repeat Exercise 6.1, but consider the design inlet angle,  $\beta_1^*$ , as the dependent variable, instead of  $i^*$ .
- 6.3 A performance analysis has been developed following the procedures of this chapter, but using Eq. (6-12) as the basis for the design incidence angle. Is there any reason to compute  $\alpha^*$  using Eq. (6-8)?